









RESEARCH ARTICLE | JULY 25 2024

Kilometer-range, full-Stokes polarimetric imaging LiDAR using fractal superconducting nanowire single-photon detectors

Yun Meng ; Kai Zou ; Zifan Hao; Song Li ; Thomas Descamps ; Adrian Iovan ; Val Zwiller ; Xiaolong Hu  

 Check for updates


Appl. Phys. Lett. 125, 041104 (2024)

<https://doi.org/10.1063/5.0218531>



View
Online


Export
Citation


20 August 2024 11:01:06




Nanotechnology &
Materials Science




Optics &
Photonics



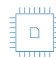
Impedance
Analysis




Scanning Probe
Microscopy



Sensors




Failure Analysis &
Semiconductors



Unlock the Full Spectrum.
From DC to 8.5 GHz.

Your Application. Measured.

[Find out more](#)



Kilometer-range, full-Stokes polarimetric imaging LiDAR using fractal superconducting nanowire single-photon detectors

Cite as: Appl. Phys. Lett. **125**, 041104 (2024); doi:10.1063/5.0218531

Submitted: 2 June 2024 · Accepted: 9 July 2024 ·

Published Online: 25 July 2024



View Online



Export Citation



CrossMark

Yun Meng,^{1,2} Kai Zou,^{1,2} Zifan Hao,^{1,2} Song Li,^{1,2} Thomas Descamps,³ Adrian Iovan,³ Val Zwiller,³ and Xiaolong Hu^{1,2,a)}

AFFILIATIONS

¹School of Precision Instrument and Optoelectronic Engineering, Tianjin University, Tianjin 300072, China

²Key Laboratory of Optoelectronic Information Science and Technology, Ministry of Education, Tianjin 300072, China

³Department of Applied Physics, Royal Institute of Technology (KTH), SE-106 91 Stockholm, Sweden

^{a)}Author to whom correspondence should be addressed: xiaolonghu@tju.edu.cn

ABSTRACT

Full-Stokes polarimetric imaging light detection and ranging (LiDAR) provides rich information about distance, materials, texture, surface orientations, and profiles of objects, and it is an important remote-sensing technology. One major challenge to reach a long distance is to efficiently collect and detect the echo photons, as for long-range LiDAR, echo photons may become sparse. Here, we demonstrate a full-Stokes polarimetric imaging LiDAR, working at the eye-safe, telecommunication wavelength of 1560 nm, that can reach a range of 4 km. The key enabling technology is a four-channel system with multimode-fiber-coupled, large-area fractal superconducting nanowire single-photon detectors. Furthermore, we also explore faster imaging (e.g., pixel-dwell time of 1 ms) of the objects at a shorter distance, approximately 1 km. Our demonstration has significantly extended the working range of full-Stokes polarimetric imaging LiDAR and represents an important step toward practical systems that may enable many applications in remote sensing and the detection and recognition of targets.

Published under an exclusive license by AIP Publishing. <https://doi.org/10.1063/5.0218531>

Light detection and ranging (LiDAR) has attracted tremendous research interest and has been used in wide applications, including autonomous vehicles, geography, atmospheric science, ecology, robotics, and spacecraft.^{1,2} In particular, photon-counting, time-of-flight (ToF) imaging LiDAR has the advantages of relatively simple hardware, low optical power, and long distance.³ By actively scanning the remote objects with light and detecting the echo photons, such a LiDAR system can present the three-dimensional profiles of objects based on the information from ToF.^{4–7} Recently, from a few kilometers^{5,8,9} to over 200 kilometers,⁷ researchers significantly extended the distances by upgrading the hardware and implementing the imaging algorithms.

In addition to the timing information, polarization is another important degree of freedom of light that can be used as a contrast for sensing^{10,11} and imaging.^{12–15} Furthermore, polarimetric LiDAR provides rich information about the aerosol types, materials, texture, surface orientations, and profiles of objects.^{16–19} Recently, we demonstrated fractal superconducting nanowire single-photon detectors (SNSPDs) that featured high detection efficiency and low polarization

sensitivity,^{20,21} and further combined the detector with a division-of-amplitude (DoA) optical system²² to perform indoor full-Stokes polarimetric imaging.¹⁹ Fractal SNSPDs can efficiently detect echo photons in any state of polarization (SoP) with high system detection efficiency (SDE), and this property further leads to being insensitive to the speckles when the fractal SNSPDs detect photons from multiple spatial modes.²³ However, further extending the distance requires high photon-collection efficiency of the optical system, in addition to high SDE of the single-photon detectors. In Ref. 19, the SNSPD was coupled with a single-mode optical fiber (SMF), which limited the collection efficiency of the echo photons due to the small receiving aperture. Additionally, only one SNSPD was used to detect photons from four output channels of the DoA system by time-multiplexing, which certainly simplified the configuration of the SNSPD cryogenic system; however, such a configuration induced additional optical losses and limited the range that the polarimetric imaging LiDAR could reach.

In this paper, we report on a full-Stokes polarimetric imaging LiDAR that can reach a range of a few kilometers, enabled by several

technological advancements in the configuration of the system. Most importantly, we used four independent, multimode-fiber (MMF)-coupled, large-area fractal SNSPDs to detect echo photons after being sorted according to their SoPs by the DoA system. Based on this SNSPD system, together with the expansion of the aperture of the telescope, effective spectral filtering and time gating to reduce noise, and extension of the raster-scanning ranges, we were able to image a remote target approximately 4 km away and obtain a complete set of polarimetric images. As the overall collection–detection efficiency was significantly enhanced, the trade-off between distance and imaging speed became relaxed, and we, therefore, also explored faster imaging with reduced pixel-dwell time in an approximately 1-km range. We believe that the photon-counting, polarimetric imaging LiDAR demonstrated in this work will find many applications such as detection and recognition of remote targets.

Figure 1(a) presents the schematics of the experimental setup of the polarimetric imaging LiDAR system. The light source was a femto-second fiber laser with a repetition rate of 82 MHz and a central wavelength of 1560 nm. The output from the laser was split by a 1/99 fiber coupler, 99% of the output went through an acousto-optic modulator (AOM), and was then collimated. The rest 1% of the output was sent to a fast photodetector with a 3-dB bandwidth of 50 GHz, to provide synchronized signals for a time-correlated single-photon counting (TCSPC) module. The divergence angle and the waist diameter of the collimated laser beam were 1 mrad and 2.1 mm, respectively. The collimated laser beam was steered by a two-stage beam-steering system that included a two-axis scanning galvo mirror for fine scanning and a motor-controlled mechanical rotational stage for coarse scanning. The galvo mirror was mounted on the stage. Figure S1 of the supplementary material presents a schematic for the two-stage raster scanning. The beam was further expanded by a 25× Newtonian telescope with an aperture size of 150 mm and a focal length of the object lens of 750 mm. The collected echo photons were split from the transmitted

beam by a 45° perforated mirror (PERM), and entered the DoA system²² for polarization analysis. The DoA system separated the incoming light into four channels, and the photon flux in each channel was proportional to the weight of the specific SoP of the incoming light:²² Ch1, Ch2, Ch3, and Ch4 were for the 0° linear SoP, the 90° linear SoP, the left-hand circular SoP, and the 135° linear SoP, respectively. The output intensity of the four channels could be expressed as the linear superposition of the four Stokes parameters of the SoP of the input light into the DoA. The coefficients of such a linear superposition formed a 4-by-4 instrument matrix. We determined the instrument matrix by a calibration procedure, as detailed in Sec. II of the supplementary material. A set of linear SoPs and SoPs on the “8”-shaped curve across the surface of the Poincaré sphere were used to calibrate the instrument matrix [Fig. S2(b) of the supplementary material].²⁴ We also tested the DoA system by using ten additional SoPs on another 8-shaped curve across the surface of the Poincaré sphere [Fig. S2(c) of the supplementary material]. The root mean square error of each normalized Stokes parameter is within 0.03. The output light from each of the four channels of the DoA system was coupled into a step-index MMF with the core diameter of 50 μm and a numerical aperture of 0.22. We used the same type of lens with the eyepiece as the coupling lens, to avoid optical aberrations.⁶

The key, enabling technology to extend the working distance of the polarimetric imaging LiDAR is a four-channel system with MMF-coupled, large-area fractal SNSPDs.²³ The coupled photons were delivered by MMFs into a cryocooler, and were further detected by the fractal SNSPDs. We used a dual-lens design^{23,25} in the detector package to boost the coupling efficiency between the MMF and each fractal SNSPD. A schematic diagram of the dual-lens package is shown in Fig. 1(b). The focal lengths of lens 1 and lens 2 were 8 and 2.98 mm, respectively, resulting in a de-magnification factor of 0.37. The focused beam size (defined as the $1/e^2$ -width of intensity distribution) was measured to be 18.3 μm,²³ which is smaller than the photo-sensitive

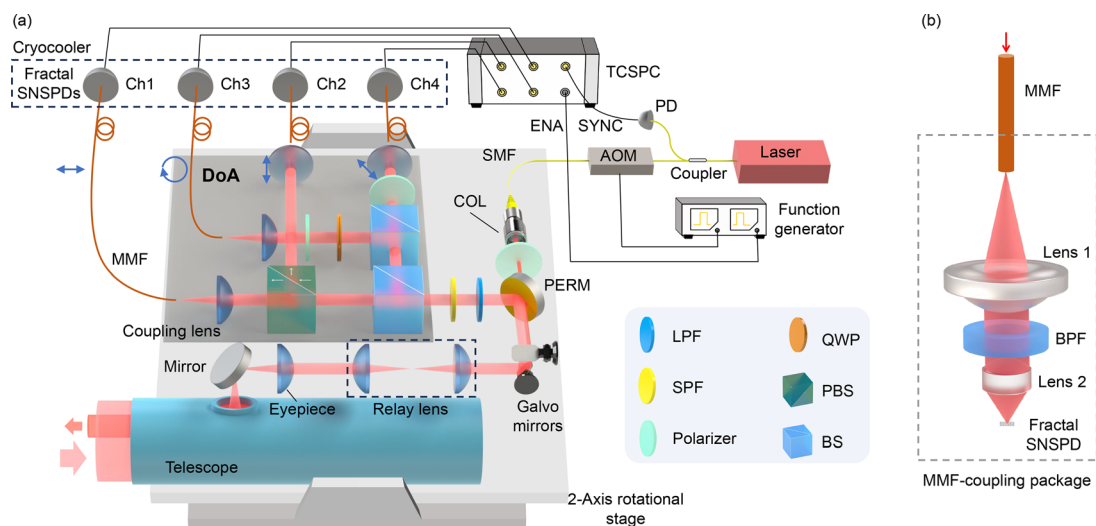


FIG. 1. Experimental setup of the full-Stokes polarimetric imaging LiDAR. (a) Schematics of the experimental setup. (b) Schematic diagram of the MMF-coupling package. AOM, acousto-optic modulator; SMF, single-mode fiber; COL, collimator; PERM, perforated mirror; LPF, long-pass filter; SPF, short-pass filter; BPF, bandpass filter; BS, non-polarizing beam splitter; PBS, polarizing beam splitter; QWP, quarter-wave plate; MMF, multimode optical fiber; SNSPD, superconducting nanowire single-photon detector; DoA, division of amplitude; PD, photodetector; SYNC, synchronizing signal; ENA, enable signal; TCSPC, time-correlated single-photon counting module.

area of the fractal SNSPDs (see Sec. III of the [supplementary material](#)). Between the two lenses was a bandpass spectral filter with a central wavelength of 1575 nm and a full-width-at-half-maxima (FWHM) bandwidth of 50 nm. The four dual-lens packages were mounted on the second stage of the 0.1-W closed-cycle Gifford–McMahon (GM) cryocooler. At the base temperature of 2.56 K, the values of SDE of the four detectors in Ch1, Ch2, Ch3, and Ch4 were $46 \pm 2\%$, $66 \pm 3\%$, $25 \pm 1\%$, and $41 \pm 2\%$, respectively. Section III of the [supplementary material](#) presents more details of the MMF-coupled fractal SNSPDs. Combining the MMF-coupled fractal SNSPDs with other techniques of spectral filtering and time gating (see Sec. IV of the [supplementary](#)

[material](#)) as well as two-stage raster scanning, our full-Stokes polarimetric imaging LiDAR reached a distance of 4 km. Table SI of the [supplementary material](#) summarizes the key parameters of our long-range polarimetric imaging LiDAR. The values of FWHM of the overall instrumental response functions of Ch1, Ch2, Ch3, and Ch4 of the polarimetric imaging LiDAR (laser pulse convoluted with the fractal SNSPD and TCSPC module) were 117, 67, 101, and 82 ps, respectively.

Using the system, we performed the full-Stokes polarimetric imaging of a building 4 km away. [Figure 2\(a\)](#) presents a satellite map of the experiment site. Our system was located on the Weijin Road

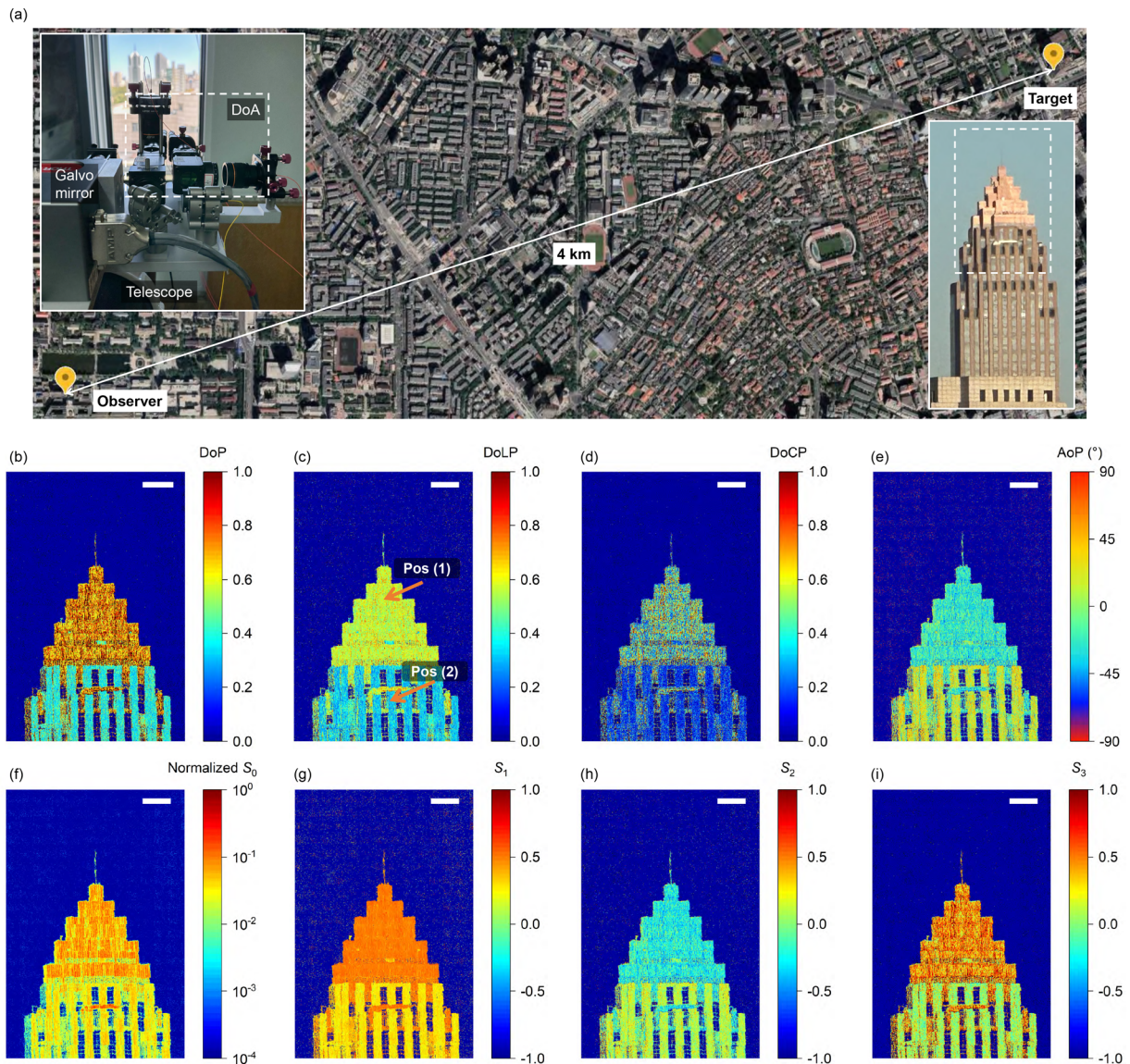


FIG. 2. Polarimetric imaging results at the distance of 4 km. (a) Satellite image of the experiment site. The insets show the photographs of the polarimetric imaging LiDAR setup (labeled as observer) and the target located at approximately 4 km away. (b) Degree of polarization (DoP) image. (c) Degree of linear polarization (DoLP) image. (d) Degree of circular polarization (DoCP) image. (e) Angle of polarization (AoP) image. (f) Normalized S_0 image. S_0 in each pixel is normalized to the maximum S_0 of all pixels. Note that this color bar is in the logarithmic scale. (g) S_1 image. (h) S_2 image. (i) S_3 image. Scale bar: 10 m.

campus of Tianjin University, and we set it up in a room on the seventh floor, with the telescope facing the window and the target. The experiment was performed at night with the pixel-dwell time of 10 ms. Figure S8(a) of the [supplementary material](#) presents the ToF imaging result. The values of depth resolution of Ch1, Ch2, Ch3, and Ch4 were 22, 11, 16, and 13 mm, respectively, and the lateral resolution was 160 mm at 4 km. [Figures 2\(b\)–2\(i\)](#) present the polarimetric imaging results. Each image, from (b) to (i), consists of 530×800 pixels. The size of each pixel is $96 \times 96 \text{ mm}^2$. The polarimetric images with the contrasts of degree of polarization [DoP, [Fig. 2\(b\)](#)], degree of linear polarization [DoLP, [Fig. 2\(c\)](#)], degree of circular polarization [DoCP, [Fig. 2\(d\)](#)], angle of polarization [AoP, [Fig. 2\(e\)](#)], S_0 [[Fig. 2\(f\)](#)], S_1 [[Fig. 2\(g\)](#)], S_2 [[Fig. 2\(h\)](#)], and S_3 [[Fig. 2\(i\)](#)] clearly show that the pyramid-shaped roof and the wall under the roof are in different colors in these images, presumably because the material of the roof is metallic and the materials of the wall under the roof include cement-like materials and glass. This observation is also evidenced by the photograph of the building, as presented in the inset of [Fig. 2\(a\)](#), which shows that the roof is in light gray and the wall is mainly in darker gray. We did get some “bad pixels” with incorrect polarimetric parameters, out of the range of definition that they should fall in. The bad pixels were due, mostly, to weak echo signals, occurring in the background space and in the region of glass windows of the building and resulting in very few coincidences. The percentage of bad pixels was 6.6%, 2.0%, 4.6%, 0, 1.8%, and 4.6% for the DoP, DoLP, DoCP, S_1 , S_2 , and S_3 images, respectively. We manually set the false color of the bad pixels black. We further took two representative locations (pixels) on the target, pos(1) and pos(2), and present the histograms of the four channels in [Figs. 3\(a\)](#) and [3\(b\)](#), respectively. The size of the coincidence window for each histogram was 1028 ps, the coincidence window was centered at the maximum of the sum of the four histograms, and the binsize of the histogram was 4 ps. The photon count of each histogram was calculated by summing all the counts in the coincidence window. Each channel in [Fig. 3\(a\)](#) shows multiple peaks because in this pixel, the surface of the target is not flat but with several steps, and the echo photons with different ToF were grouped into several peaks, accordingly.

We also performed faster polarimetric imaging of a remote object at a shorter distance, 1.05 km, by reducing pixel-dwell time. The target was a television tower, mainly made of metals, on top of a building. Figure S8(b) of the [supplementary material](#) presents the ToF imaging result. [Figures 4\(a\)](#), [4\(b\)](#), [4\(c\)](#), and [4\(d\)](#) present the obtained images with the contrast of DoP for pixel-dwell time of 100, 10, 5, and 1 ms, respectively. Images with other polarimetric contrasts were also obtained. As expected, the signal-to-noise ratio (SNR) is perceptually reducing with reducing the pixel-dwell time; however, the profile of the tower is still clearly outlined even with a 1-ms pixel-dwell time. Quantitatively, we used the image with 100-ms pixel-dwell time as the ground truth (GT), and compared the rest three with a shorter pixel-dwell time with the GT. [Figure 4\(e\)](#) presents the root mean square error of the normalized Stokes parameter, $\Delta_{\bar{S}} = \sqrt{\Delta_{S_1}^2 + \Delta_{S_2}^2 + \Delta_{S_3}^2} / \sqrt{3}$, where $\Delta_{S_N} = \sum_{i,j \in \mathbb{A}} |S_N^{(i,j)} - S_N^{(i,j)}| / |\mathbb{A}|$, $N = 1, 2, 3$ and \mathbb{A} is the set of pixels whose S_1 , S_2 , and S_3 are in the range $[-1, 1]$. The pixels whose S_1 , S_2 , and S_3 fall out of the range $[-1, 1]$ only contribute a small percentage ($< 2.8\%$) of the total pixels. As we reduced the pixel-dwell time, the deviations from the GT increased. [Figure 4\(f\)](#) presents the detected photons per pixel (ppp) for each pixel-dwell time,

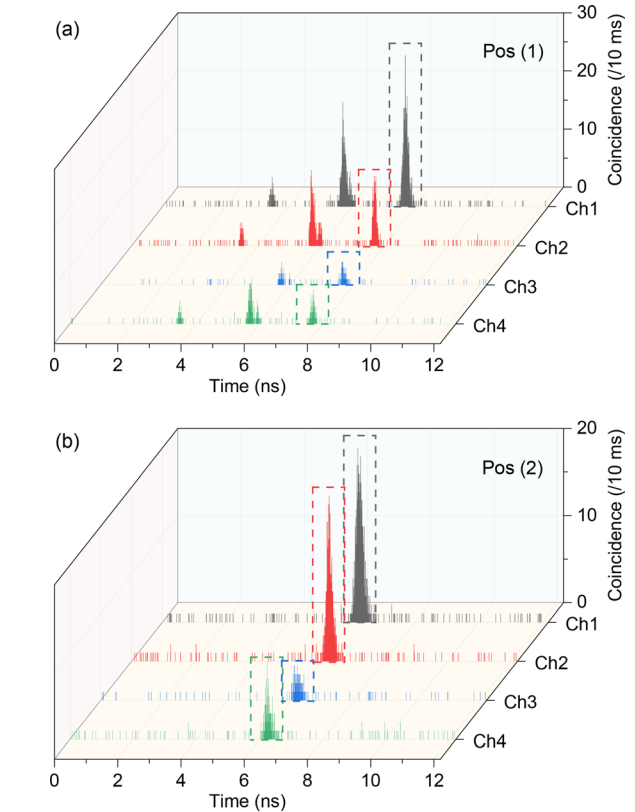


FIG. 3. Representative time-of-flight histograms of the 4-km polarimetric imaging. (a) ToF histograms in the four channels of the pixel at position 1, as pointed in [Fig. 2\(c\)](#). (b) ToF histograms in the four channels of the pixel at position 2, as pointed in [Fig. 2\(c\)](#). The coincidences in the dashed boxes were used for calculating the polarimetric parameters.

$$ppp = \sum_{i=1}^{80} \sum_{j=1}^{181} \sum_{k=1}^4 PC_{i,j,k} / 80 / 181$$
, where $PC_{i,j,k}$ is the photon count at the pixel (i, j) of the channel k . Therefore, the trade-off between imaging speed and SNR still existed, but the enhanced overall collection–detection efficiency of the echo photons to a large extent mitigated this trade-off. Compared with the initial indoor demonstration of the full-Stokes polarimetric imaging LiDAR,¹⁹ we estimated that the overall collection–detection efficiency of echo photons was improved by 37 dB in this work. Section VII of the [supplementary material](#) details the comparison. In the future, it is possible to operate our polarimetric imaging LiDAR in daylight, provided that a narrow bandpass spectral filter in the dual-lens package and a narrower-linewidth pulsed laser were used.

In conclusion, we have demonstrated a kilometer-range, full-Stokes polarimetric imaging system that includes four MMF-coupled fractal SNSPDs. Using this system, we have imaged an object 4 km away and have obtained a complete set of polarimetric images. Compared with the initial demonstration of full-Stokes polarimetric LiDAR working indoors in a range of a few meters, we have enhanced the overall collection–detection efficiency of the echo photons and have thereby extended the working range. We believe that this work represents an important step toward practical photon-counting polarimetric imaging LiDAR systems that may find applications in the

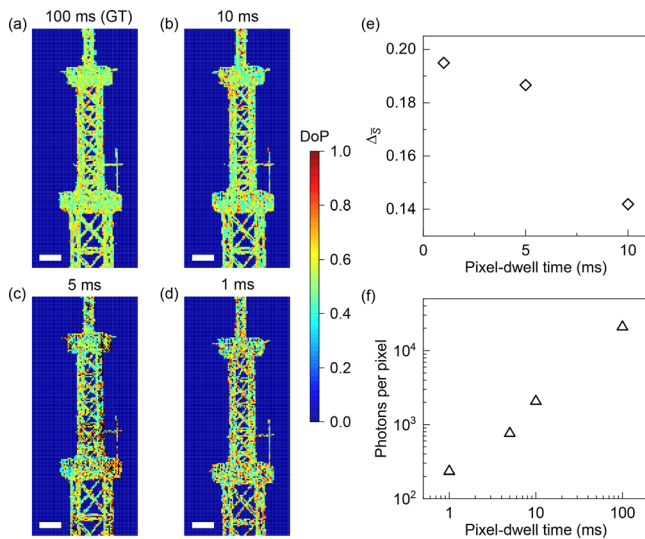


FIG. 4. Polarimetric imaging results at the distance of 1.05 km with short pixel-dwell time. (a)–(d) DoP image with the pixel-dwell time of 100, 10, 5, and 1 ms, respectively. Scale bar: 2 m. The image with pixel-dwell time of 100 ms serves as the ground truth (GT). (e) Root mean square error of the normalized Stokes parameter at several pixel-dwell times. (f) Detected photons per pixel (ppp) at several pixel-dwell times.

detection and recognition of remote targets with rich profiles and material information.

See the [supplementary material](#) for the two-stage beam steering, the calibration of instrument matrix, more details about the multi-mode-fiber-coupled fractal SNSPDs, the spectral filtering and time gating, the key parameters of the polarimetric imaging LiDAR, the time-of-flight imaging results, and the enhancement of overall efficiency in comparison with previous work.

The authors acknowledge funding from the Innovation Program for Quantum Science and Technology (No. 2023ZD0300100) and the National Natural Science Foundation of China (No. 62071322). Portions of this work were submitted to CLEO 2024.

AUTHOR DECLARATIONS

Conflict of Interest

The authors have no conflicts to disclose.

Author Contributions

Yun Meng and Kai Zou contributed equally to this work.

Yun Meng: Conceptualization (equal); Data curation (lead); Formal analysis (lead); Investigation (lead); Methodology (lead); Software (lead); Validation (equal); Visualization (equal); Writing – original draft (equal); Writing – review & editing (equal). **Kai Zou:** Conceptualization (equal); Data curation (lead); Formal analysis (lead); Investigation (lead); Methodology (lead); Software (lead); Validation (equal); Visualization (equal); Writing – original draft

(equal); Writing – review & editing (equal). **Zifan Hao:** Data curation (supporting); Writing – original draft (supporting); Writing – review & editing (supporting). **Song Li:** Data curation (supporting); Writing – original draft (supporting); Writing – review & editing (supporting). **Thomas Descamps:** Resources (supporting); Writing – review & editing (supporting). **Adrian Iovan:** Resources (supporting); Writing – review & editing (supporting). **Val Zwiller:** Resources (supporting); Writing – review & editing (supporting). **Xiaolong Hu:** Conceptualization (lead); Data curation (equal); Formal analysis (equal); Funding acquisition (lead); Investigation (equal); Methodology (equal); Project administration (lead); Resources (lead); Software (equal); Supervision (lead); Validation (equal); Visualization (equal); Writing – original draft (equal); Writing – review & editing (equal).

DATA AVAILABILITY

The data that support the findings of this study are available from the corresponding author upon reasonable request.

REFERENCES

- 1B. Schwarz, “Mapping the world in 3D,” *Nat. Photonics* **4**, 429–430 (2010).
- 2T. Markus, T. Neumann, A. Martino, W. Abdalati, K. Brunt, B. Csatho, S. Farrell, H. Fricker, A. Gardner, D. Harding, M. Jasinski, R. Kwok, L. Magruder, D. Lubin, S. Luthcke, J. Morison, R. Nelson, A. Neuenschwander, S. Palm, S. Popescu, C. Shum, B. E. Schutz, B. Smith, Y. Yang, and J. Zwally, “The Ice, Cloud, and Land Elevation Satellite-2 (ICESat-2): Science requirements, concept, and implementation,” *Remote Sens. Environ.* **190**, 260–273 (2017).
- 3R. H. Hadfield, J. Leach, F. Fleming, D. J. Paul, C. H. Tan, J. S. Ng, R. K. Henderson, and G. S. Buller, “Single-photon detection for long-range imaging and sensing,” *Optica* **10**, 1124–1141 (2023).
- 4R. E. Warburton, A. McCarthy, A. M. Wallace, S. Hernandez-Marin, R. H. Hadfield, S. W. Nam, and G. S. Buller, “Subcentimeter depth resolution using a single-photon counting time-of-flight laser ranging system at 1550 nm wavelength,” *Opt. Lett.* **32**, 2266–2268 (2007).
- 5A. M. Pawlikowska, A. Halimi, R. A. Lamb, and G. S. Buller, “Single-photon three-dimensional imaging at up to 10 kilometers range,” *Opt. Express* **25**, 11919–11931 (2017).
- 6Z.-P. Li, X. Huang, Y. Cao, B. Wang, Y.-H. Li, W. Jin, C. Yu, J. Zhang, Q. Zhang, C.-Z. Peng, F. Xu, and J.-W. Pan, “Single-photon computational 3D imaging at 45 km,” *Photonics Res.* **8**, 1532–1540 (2020).
- 7Z.-P. Li, J.-T. Ye, X. Huang, P.-Y. Jiang, Y. Cao, Y. Hong, C. Yu, J. Zhang, Q. Zhang, C.-Z. Peng, F. Xu, and J. Pan, “Single-photon imaging over 200 km,” *Optica* **8**, 344–349 (2021).
- 8A. McCarthy, X. Ren, A. Della Frera, N. R. Gemmill, N. J. Krichel, C. Scarcella, A. Ruggeri, A. Tosi, and G. S. Buller, “Kilometer-range depth imaging at 1550 nm wavelength using an InGaAs/InP single-photon avalanche diode detector,” *Opt. Express* **21**, 22098–22113 (2013).
- 9A. McCarthy, N. J. Krichel, N. R. Gemmill, X. Ren, M. G. Tanner, S. N. Dorenbos, V. Zwiller, R. H. Hadfield, and G. S. Buller, “Kilometer-range, high resolution depth imaging via 1560 nm wavelength single-photon detection,” *Opt. Express* **21**, 8904–8915 (2013).
- 10M. F. Sterzik, S. Bagnulo, and E. Palle, “Biosignatures as revealed by spectropolarimetry of Earthshine,” *Nature* **483**, 64–66 (2012).
- 11C. He, H. He, J. Chang, B. Chen, H. Ma, and M. J. Booth, “Polarisation optics for biomedical and clinical applications: A review,” *Light: Sci. Appl.* **10**, 194 (2021).
- 12A. Carnicer and B. Javidi, “Polarimetric 3D integral imaging in photon-starved conditions,” *Opt. Express* **23**, 6408–6417 (2015).
- 13N. A. Rubin, G. D’Aversa, P. Chevalier, Z. Shi, W. T. Chen, and F. Capasso, “Matrix Fourier optics enables a compact full-Stokes polarization camera,” *Science* **365**, eaax1839 (2019).
- 14S.-H. Baek and F. Heide, “All-photon polarimetric time-of-flight imaging,” in *CVPR* (IEEE Computer Society, 2022), pp. 17876–17885.

- ¹⁵J. Zuo, J. Bai, S. Choi, A. Basiri, X. Chen, C. Wang, and Y. Yao, "Chip-integrated metasurface full-Stokes polarimetric imaging sensor," *Light: Sci. Appl.* **12**, 218 (2023).
- ¹⁶J. Qiu, H. Xia, M. Shangguan, X. Dou, M. Li, C. Wang, X. Shang, S. Lin, and J. Liu, "Micro-pulse polarization LIDAR at 1.5 μm using a single superconducting nanowire single-photon detector," *Opt. Lett.* **42**, 4454–4457 (2017).
- ¹⁷Y. Chen, K. Yin, D. Shi, W. Yang, J. Huang, Z. Guo, K. Yuan, and Y. Wang, "Detection and imaging of distant targets by near-infrared polarization single-pixel LIDAR," *Appl. Opt.* **61**, 6905–6914 (2022).
- ¹⁸X.-Q. Sun, W.-J. Zhang, C.-J. Zhang, L.-X. You, G.-Z. Xu, J. Huang, H. Zhou, H. Li, Z. Wang, and X.-M. Xie, "Polarization resolving and imaging with a single-photon sensitive superconducting nanowire array," *Opt. Express* **29**, 11021–11036 (2021).
- ¹⁹N. Hu, Y. Meng, K. Zou, Y. Feng, Z. Hao, S. Steinhauer, S. Gyger, V. Zwiller, and X. Hu, "Full-Stokes polarimetric measurements and imaging using a fractal superconducting nanowire single-photon detector," *Optica* **9**, 346–351 (2022).
- ²⁰Y. Meng, K. Zou, N. Hu, L. Xu, X. Lan, S. Steinhauer, S. Gyger, V. Zwiller, and X. Hu, "Fractal superconducting nanowires detect infrared single photons with 84% system detection efficiency, 1.02 polarization sensitivity, and 20.8 ps timing resolution," *ACS Photonics* **9**, 1547–1553 (2022).
- ²¹K. Zou, Z. Hao, Y. Feng, Y. Meng, N. Hu, S. Steinhauer, S. Gyger, V. Zwiller, and X. Hu, "Fractal superconducting nanowire single-photon detectors working in dual bands and their applications in free-space and underwater hybrid LIDAR," *Opt. Lett.* **48**, 415–418 (2023).
- ²²R. Azzam, "Division-of-amplitude photopolarimeter (DOAP) for the simultaneous measurement of all four Stokes parameters of light," *Opt. Acta* **29**, 685–689 (1982).
- ²³K. Zou, Y. Meng, Z. Hao, S. Li, A. Iovan, T. Descamps, V. Zwiller, and X. Hu, "Speckle-insensitive fractal superconducting nanowire single-photon detector coupled with multimode optical fiber," *Laser Photonics Rev.* 2400342 (2024).
- ²⁴C. He, J. Chang, Y. Wang, R. Liao, H. He, N. Zeng, and H. Ma, "Linear polarization optimized Stokes polarimeter based on four-quadrant detector," *Appl. Opt.* **54**, 4458–4463 (2015).
- ²⁵L. Zhang, C. Wan, M. Gu, R. Xu, S. Zhang, L. Kang, J. Chen, and P. Wu, "Dual-lens beam compression for optical coupling in superconducting nanowire single-photon detectors," *Sci. Bull.* **60**, 1434–1438 (2015).